Vortex light bullets in Rydberg atoms trapped in twisted $\mathcal{PT}$-symmetric waveguide arrays

Siliu Xu,[1,2] Junhao Li,[1,3] Yiheng Hou,[1,3] Jun-Rong He,[1,3] Zhou Fan,[1,2] Yuan Zhao,[1,2,*] and Liangwei Dong[4,†]

[1]*Key Laboratory of Optoelectronic Sensing and Intelligent Control, Hubei University of Science and Technology, Xianning 437100, China*

[2]*School of Biomedical Engineering and Imaging, Xianning Medical College, Hubei University of Science and Technology, Xianning 437100, China*

[3]*School of Electronic and Information Engineering, Hubei University of Science and Technology, Xianning 437100, China*

[4]*Department of Physics, Zhejiang University of Science and Technology, Hangzhou 310023, China*

(Received 2 April 2024; accepted 18 July 2024; published 6 August 2024)

We present a theoretical scheme for generating vortex light bullets (LBs) in a Rydberg atomic system. The stability property and propagation dynamics of vortex LBs with different topological charges are investigated in twisted circular waveguide arrays with a parity-time ($\mathcal{PT}$) symmetry. The numerical solutions of the corresponding nonlinear Schrödinger equation are obtained by the modified square operator method and split-step Fourier method. The longitudinal twist changes the stabilities of six-core vortex LBs and enriches the modulation diversity as the states with the opposite charges degenerate by the introducing of rotation frequency. Specifically, we reveal that the energy exchange between waveguides and media gives rise to the formation of necklace breathers, which is crucial for implementing light storage. These unique characteristics arise from the balance or quasibalance among the rotation frequency, the Rydberg-Rydberg interaction, and the nonequivalent gain/loss distribution along the azimuthal direction. We thus provide examples of robust high-charge vortex LBs and necklace breathers in the Rydberg atomic system with a $\mathcal{PT}$ symmetry.

DOI: 10.1103/PhysRevA.110.023508

I. INTRODUCTION

Light bullets (LBs) are maintained due to the balance between dispersion, diffraction, and nonlinear effects [1]. LBs have been observed in various physical systems, including nonlinear optics, plasmas, and Bose-Einstein condensates [2–5]. These nonlinear waves play a crucial role in optical communication, high-speed data processing, and quantum information technology [6–8], making them a topic of significant theoretical and experimental interest. However, the experimental realization of LBs faces several challenges. The major challenge lies in achieving a balance among the diffraction, dispersion, and nonlinearity [9,10]. In uniform media, LBs are typically unstable because the common Kerr nonlinearity leads to supercritical collapse [1,11].

The formation of LBs has been studied through various theoretical proposals, including nonlinear optical materials with spatially patterned nonlinear interactions [12], optical tandem systems [13], materials with saturable and quadratic nonlinearities [14,15], and combinations of local and nonlocal optical nonlinearities [16,17]. LBs have also been investigated in dissipative settings, where higher-order absorption commonly occurs [18,19]. Recently, the Rydberg electromagnetically induced transparency (Rydberg-EIT) system has emerged as a promising setting for generating stable LBs [20–22]. In Rydberg-EIT systems, the cold atomic gas becomes an effective alternative for the formation, propagation, and storage of ultraslow weak LBs and vortices [23–26].

A powerful strategy for achieving stable LBs is the introduction of spatial modulations of refractive index. The existence of stable fundamental LBs in discrete [27] and continuous [28,29] lattices, as well as vortex LBs [30,31], has been predicted. This approach has led to the experimental observation of fundamental LBs in fiber arrays [32,33] and, subsequently, the observation of discrete vortex LBs [34]. In the context of communication, vortex LBs are particularly significant as they carry nonzero angular momentum. However, vortex LBs often experience strong azimuthal instability, leading to the fragmentation of vortex rings in two-dimensional (2D) [26,35] and three-dimensional (3D) nonlinear systems [25]. More recently, a proposal utilizing twisted waveguide arrays has been reported, demonstrating the stability of LBs [36,37]. The twisting of fiber arrays provides a powerful way that changes the properties of LBs, resulting in stable LBs without an energy threshold.

Previous studies on LBs are solely based on transverse refractive-index modulation. Recently, the $\mathcal{PT}$-symmetric system with entirely real eigenvalues has extended the quantum theory to complex domains, where the Hamiltonian is non-Hermitian [38–43]. Unlike the Hermitian Hamiltonian which guarantees the energy spectrum to be real, the non-Hermitian Hamiltonian usually has complex spectrum. Bender and Boettcher [44,45] proved that all-real spectra may appear for a broad class of Hamiltonians which are not-Hermitian but invariant under the transformations of parity ($\mathcal{P}$) and time ($\mathcal{T}$) inversions, i.e., $\mathcal{PT}$ symmetry. If the $\mathcal{PT}$ symmetry does not hold, the broken $\mathcal{PT}$ symmetry will result

*Contact author: yuanuanz@163.com
†Contact author: dlw_0@163.com

in the presence of complex eigenvalues. The $\mathcal{PT}$ symmetry breaking and the associated change from real to complex eigenvalues can be generally observed when the gain or loss of the system is changed.

Interestingly, $\mathcal{PT}$-symmetric photonic structures have been shown to support stable LBs by preventing the collapse of spatial 2D solitons [46–48] and 3D LBs [25,49]. The dynamical characteristics of fundamental and vortex LBs were studied in focusing Kerr media modulated by complex $\mathcal{PT}$-symmetric periodic lattices. The imaginary part of the lattice creates strong internal currents in LBs, significantly affecting their existence and stability domains [50].

Thus far, 2D vortex solitons have been studied in $\mathcal{PT}$-symmetric azimuthal potentials [51] and twisted circular waveguide arrays [37,52,53]. Stable 3D vortex LBs have been predicted in Rydberg atomic systems [25] and Kerr nonlinear optical media [42]. It should be noted that all previous studies on LBs are based on transverse refractive-index modulation. Moreover, vortex LBs can be stable only for charges $m \leqslant 2$. The existence and propagation dynamics of 3D vortex LBs in rotating azimuthal potentials, composed of $\mathcal{PT}$-symmetric cells located on a ring, have not been explored. Additionally, it is unknown whether stable 3D vortex LBs can be achieved through a combination of Rydberg-Rydberg interaction and $\mathcal{PT}$-symmetric azimuthal potentials. In this paper, we predict an example of robust vortex LBs forming in Rydberg-EIT $\mathcal{PT}$-symmetric circular waveguide arrays within a coherent atomic gas.

This paper is structured as follows. The theoretical model is presented in Sec. II. Numerical results and discussions about the six-core vortex LBs are presented in Sec. III. A summary is provided in Sec. IV. The propagation of six-core vortex LBs with a value of $m = -2$ is outlined in the Supplemental Material, Movie 1 [54]. The evolutions of eight-core counterparts with $m = -2$ and -3 are included in the Supplemental Material, Movies 2 and 3, respectively [54]. The modulation of eight-core vortex LBs is presented in the Supplemental Material, Movie 4 [54]. The Supplemental Material is summarized in Ref. [54].

II. THE MODEL

We adopt a cold four-level atomic system with an inverted-Y type configuration. The supposed geometry and energy level structure are depicted in Figs. 1(a) and 1(b), respectively. The pulsed probe (with frequency ω_p and half Rabi frequency Ω_p) and control (with frequency ω_c and half Rabi frequency Ω_c) laser fields are coupled to the transitions $|1\rangle \rightarrow |3\rangle$ and $|2\rangle \rightarrow |3\rangle$, where Γ_{ij} are spontaneous emission decay rates between states $|i\rangle$ and $|j\rangle$. This EIT structure is dressed by a high-lying Rydberg state $|4\rangle$, which is coupled by the auxiliary field (with frequency ω_a and half Rabi frequency Ω_a). $\Delta_3 = \omega_p - (\omega_3 - \omega_1)$ is one-photon detuning, and $\Delta_2 = \omega_p - \omega_c - (\omega_2 - \omega_1)$ and $\Delta_4 = \omega_p + \omega_a - (\omega_4 - \omega_1)$ are two-photon detunings. An incoherent pumping (with pumping rate Γ_{21}) is used to pump atoms $|1\rangle \rightarrow |2\rangle$, providing a gain for the probe field.

Under the slowly varying amplitude approximation, the nonlinear Schrödinger equation for the probe field takes the form [23]

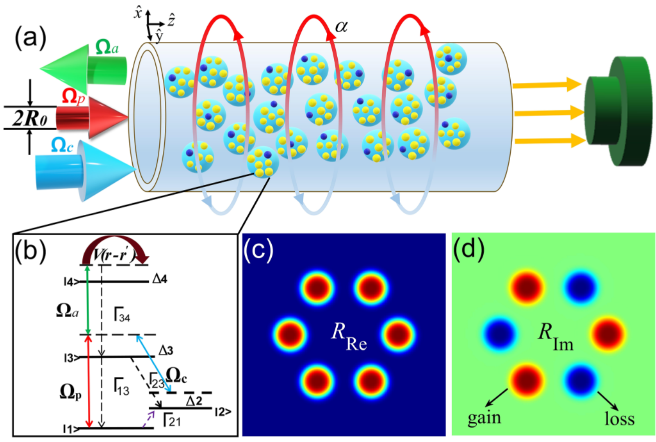

FIG. 1. (a) Schematic for the experimental demonstration. A Rydberg-dressed atom is driven by a weak probe field, Ω_p; an auxiliary field, Ω_a; and a strong control field, Ω_c. Here Γ_{ij} are the spontaneous emission decay rates from $|l\rangle$ to $|j\rangle$ ($j, l = 1, \ldots, 4$), and Δ_j are the corresponding detunings. (b) Level diagram and excitation scheme of the four-level Rydberg-EIT system. (c), (d) Profiles of real and imaginary parts of six-core waveguide potential at $z = 0$.

$$i\frac{\partial \psi}{\partial z} = -\frac{1}{2}\Delta\psi - R(\mathbf{r}, z)\psi - |\psi|^2\psi - \int d^2\mathbf{r}' V_{\mathrm{vdw}}(\mathbf{r}' - \mathbf{r})|\psi|^2\psi, \tag{1}$$

where $\Delta = \partial^2/\partial x^2 + \partial^2/\partial y^2 + \partial^2/\partial \tau^2$, $\mathbf{r} \rightarrow \{x, y\}/r_0$ are the normalized transverse coordinates with $r_0 = 10$ μm being the typical radius of the probe beam, and $z \rightarrow z/L_{\mathrm{diff}}$ is the normal transverse coordinate with $L_{\mathrm{diff}} = kr_0^2$ being the diffraction length. We suppose the light (with wavelength $\lambda = 760$ nm and wave number $k = 2\pi n/\lambda$) propagates in the material (with refractive index $n \approx 1.45$), and thus the diffraction length $L_{\mathrm{diff}} = 1.2$ mm. $\tau = t/\tau_0$ is the scaled time coordinate with τ_0 being the initial Rabi frequency of the probe pulse. It is noted that this is a continuum model, where the wave function ψ can be used to describe the system. Under the anticontinuum limit, Eq. (1) can be reduced to a system of coupled mode equations with $\psi_n (n = 1, \ldots, N)$, where each mode couples with its neighbors [55–58].

The external potential $R(\mathbf{r}, z)$ has a complex form that is constructed by N single-mode super-Gaussian waveguides,

$$R = \sum_{l=1}^{\mathrm{N}} (p_r + i^{2l+1} p_i) e^{-[(x-x_l)^2 + (y-y_l)^2]^2/w^4}, \tag{2}$$

where p_r and p_i represent the strengths of real and imaginary parts, respectively; N is the core number of the super-Gaussian beams; and w is the beam width chosen as $w = 0.5$ (5 μm). The coordinates of the core centers on the ring are $x_l = \rho\cos\phi_l$ and $y_l = \rho\sin\phi_l$, where ρ is the radius of ring (set to be 1) and $\phi_l = 2\pi(l-1)/N$. The potential is $\mathcal{PT}$-symmetric, satisfying $R(\mathbf{r}) = R^*(-\mathbf{r})$, and can be obtained by modulating the control and auxiliary fields [41] as follows:

$$\frac{\Omega_c}{\Omega_{c0}} \approx 1 + 0.25 \sum_{l=1}^{N} i^{2l} p_i e^{-[(x-x_l)^2+(y-y_l)^2]^2/w^4},$$

$$\frac{\Omega_a}{\Omega_{a0}} \approx 1 + 0.43 \sum_{l=1}^{N} (p_r - 0.65 p_i) e^{-[(x-x_l)^2+(y-y_l)^2]^2/w^4}, \quad (3)$$

where Ω_{c0} and Ω_{a0} are the initial half Rabi frequencies of control and auxiliary fields, respectively.

The last term in Eq. (1) is the long-range interaction between different Rydberg atoms with the van der Waals potential $V_{\mathrm{vdw}} = \hbar V(\mathbf{r}' - \mathbf{r})$, where $V(\mathbf{r}' - \mathbf{r}) = C_6/[R_b^6 + |\mathbf{r}' - \mathbf{r}|^6]$, $C_6 < 0$ is the dispersion parameter, $\mathbf{r}$ and $\mathbf{r}'$ are vector positions of two Rydberg atoms, and R_b is the Rydberg blockade radius which can be obtained as $R_b = [|C_6\Delta_3|/|\Omega_c|^2]^{1/6}$. The degree of the nonlocality is determined by the parameter $\sigma = R_b/r_0$. By adjusting the values of R_b and r_0, the nonlinear system displays three kinds of localized regions: local region ($\sigma \ll 1$), general nonlocal region ($\sigma \sim 1$), and strongly nonlocal region ($\sigma \gg 1$) [25].

Suppose the waveguide arrays have a longitudinal twist with rotation frequency α, then x_l and y_l satisfy the following rotating relation with the propagation distance z:

$$x_l(z) = x\cos(\alpha z) - y\sin(\alpha z),$$
$$y_l(z) = x\sin(\alpha z) + y\cos(\alpha z). \quad (4)$$

Thus, Eq. (1) is transformed to the following expression:

$$i\frac{\partial \psi}{\partial z} = -\frac{1}{2}\Delta\psi - \alpha L_z \psi - R(\mathbf{r})\psi - |\psi|^2\psi - \int d^2\mathbf{r}' V_{\mathrm{vdw}}(\mathbf{r}' - \mathbf{r})|\psi|^2\psi. \quad (5)$$

The rotating operator $\alpha L_z = i\alpha(x\partial/\partial y - y\partial/\partial x)$ does not change the original $\mathcal{PT}$ symmetry since the derivative is invariant under rotation $\phi_k \to \phi_k - 2\pi/N$. The rotating operator can be regarded as an effective Coriolis force if one considers the beam field as a rigid body. The Coriolis force also denotes the "artificial" angular momentum induced by the rotation of the potential. It plays a role in accelerating or slowing the internal energy flux of the beams with angular momenta. Our study focuses on analyzing six-core structures, as depicted in Figs. 1(c) and 1(d), where each core exhibits gain or loss. To achieve the desired rotation setup, the rotation frequency of the container housing cold Rydberg atoms should be small ($0 \leqslant \alpha < 0.4$), and the optimal value is $\alpha = 0.1$. As a result, the original $\mathcal{PT}$ symmetry remains invariant within the rotational coordinate system.

For experimental consideration, this rotation system can be realized in a cold gas of ^{88}Sr atoms [21,25]. Thus, the relevant values of the physical parameters are $r_0 = 10$ μm, $\tau_0 = 1.1$ μs, $\Gamma_{21} = 0.2\pi$ MHz, $\Gamma_3 = 2\pi \times 16$ MHz, $\Gamma_4 = \Gamma_{34} = 2\pi \times 16.7$ kHz, $C_6 = 2\pi \times 81.6$ GHz μm^6, $\Delta_2 = 1.67 \times 10^6$ s^{-1}, $\Delta_3 = 9.67 \times 10^7$ s^{-1}, $\Delta_4 = 1.36 \times 10^7$ s^{-1}, $\Omega_c = \Omega_{c0} = 1.2 \times 10^7$ s^{-1}, and $\Omega_a = \Omega_{a0} = 5 \times 10^6$ s^{-1}. The units of the scaled propagation distance and time are 1.2 mm and 1.1 μm, corresponding to $z = 1$ and $t = 1$, respectively. The unit for softcore size is estimated as $R_b \sim 8.6$ μm [25].

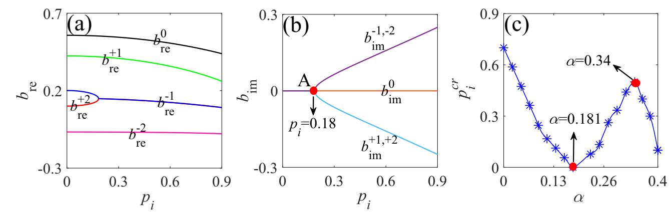

FIG. 2. (a), (b) Linear spectrum of b with superscript ±1 and 2 representing the topological charge. Here, panels (a) and (b) represent the real and imaginary parts of b. (c) Critical value of p_i with increasing α in the linear condition. Point A in panel (b) stands for the critical point where b turns to complex. The fixed parameters in the panels are $p_r = 3$, $p_i = 0.1$, $\sigma = 2.5$, and $\alpha = 0.15$.

III. NUMERICAL RESULTS AND DISCUSSIONS

Vortex solitons can be sought in the form $\psi = \varphi(x, y, \tau)e^{im\theta + ibz}$, where $\varphi(x, y, \tau)$ is the stationary solution, m is the topological charge of the angular mode, θ is the azimuthal angle, and b is the propagation constant. In the numerical calculation, the initial condition is selected as

$$\varphi_0 = A\left(\frac{\sqrt{x^2 + y^2}}{w_0}\right)^{|m|} e^{-\frac{(x-x_0)^2+(y-y_0)^2+(\tau-\tau_0)^2}{w_0^2}}, \quad (6)$$

where the initial amplitude $A = 1$, the width of laser beam $w_0 = 0.5$ (standing for 5 μm), and the beam center $(x_0, y_0, \tau_0) = (0, 0, 0)$. We substitute the initial solution $\psi_0 = \varphi_0 e^{im\theta + ibz}$ into Eq. (5), and the vortex solutions are obtained by means of the modified square operator method [59]. Vortex LBs with six-core and various topological charges ($m = \pm1, \pm2$) are found in this 3D rotating system with Rydberg atoms, satisfying the charge rule $m < N/2$ [60].

A. Modulation and characteristics of six-core vortex LBs

Upon the removal of the Kerr local nonlinearity and Rydberg-induced nonlocal nonlinearity from Eq. (5), the equation transforms into a linear equation with an infinite number of eigenvalues and associated linear eigenmodes. In cases where nonlinearity cannot be ignored, nonlinear modes can bifurcate from linear modes. Linear modes intuitively reveal the possible profiles of nonlinear modes originating from them [61].

The dispersion relation with the given super-Gaussian potential is depicted in Fig. 2(a). One observes that the linear spectra of the six-core system experience a breaking of $\mathcal{PT}$ symmetry. Two branches of b_{re} (with $m = \pm1$ and $m = \pm2$) merge at a critical value, $p_i^{\mathrm{cr}} = 0.18$ (labeled with point A). Actually in the dispersion relation, more eigenvalues b corresponding to $|m| > 2$ can be obtained, but they have complex values and the corresponding LBs are unstable. They are not plotted in Fig. 2(a). Beyond point A, the imaginary part b_{im} splits into two branches from zero, indicating the change from real to complex eigenvalues. This transition is usually denoted as the $\mathcal{PT}$ symmetry breaking for the non-Hermitian system. Further, the complex eigenvalues with $m = \pm1$ are always conjugate to those with $m = \pm2$ [52].

The critical value p_i^{cr} of the symmetry-breaking point changes quasiperiodically with the rotation frequency α, as shown in Fig. 2(c). The $\mathcal{PT}$-symmetric structure is partly

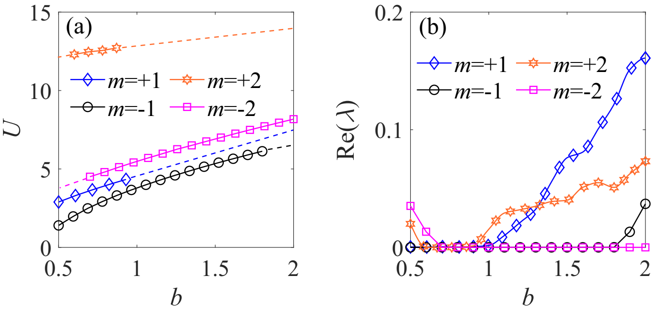

FIG. 3. (a) Power of vortex LBs vs propagation constant b, where the solid and dashed lines represent the robust and unstable states. (b) Real part of λ with respect to b. The fixed parameters in the panels are $p_r = 3$, $p_i = 0.1$, $\sigma = 2.5$, and $\alpha = 0.15$.

affected by the rotation of waveguide arrays, resulting in the decrease of $p_i^{\rm cr}$. However, when the rotation frequency α exceeds an inflection point ($\alpha = 0.181$), the $p_i^{\rm cr}$ values increase with α and reach the second maximum value at $\alpha = 0.34$ due to the rotation invariant with $\phi_k \to \phi_k - 2\pi/N$.

The power of vortex LBs, defined as $U = \iiint |\psi|^2 {\rm d}x{\rm d}y{\rm d}\tau$, is shown in Fig. 3(a) with respect to the propagation constant b. The robust and unstable states of vortex LBs are plotted by solid and dashed segments, respectively. The results show that the power of vortices with larger topological charges (e.g., $m = +2$) is greater than that of those with smaller topological charges (e.g., $m = +1$), and vortices with positive m have U values larger than those of vortices with negative m.

The instability growth rate of these vortex LBs is calculated by the linear stability analysis by introducing weak perturbation $\psi = (\varphi + pe^{\lambda t} + q^* e^{\lambda^* t})e^{im\theta + ibz}$, where p and q are small perturbations with $|p, q| \ll |\varphi|$, the symbol $*$ represents the complex conjugation, and λ's are the complex eigenvalues standing for the instability growth rate of the disturbation. λ can be obtained by substituting ψ into Eq. (5) and linearizing it around the stationary solution. The vortex LBs can propagate stably when ${\rm Re}(\lambda) = 0$. The spectrum of ${\rm Re}(\lambda)$ in Fig. 3(b) indicates that the stability domain of vortex LBs with positive topological charges ($m = +1$ and $+2$) are smaller than the ones with negative charges ($m = -1$ and -2). The stability domains of b given by Figs. 3(a) and 3(b) are [0.5 0.93], [0.5 1.8], [0.6 0.87], and [0.7 2.0] for $m = +1$, -1, $+2$, and -2, respectively. Here the real part of instability growth rate is of the order of 10^{-3} in the simulation, i.e., ${\rm Re}(\lambda) < 10^{-3}$. The real part of λ in Fig. 3(b) appears to be very close to zero; however, it is not exactly zero. Even within the stability domains, the vortex LBs can be generated stably but may not propagate for a long distance.

The stability domains in nonlinear conditions can be tuned by varying the imaginary part of the potential p_i, the degree of nonlocal nonlinearity σ, and the rotation frequency α, as shown in Fig. 4. The $\mathcal{PT}$ symmetry can be obtained in the scope of $[b_{\rm cr}^{\rm low}, b_{\rm cr}^{\rm upp}]$, shown in Figs. 4(a), 4(c), and 4(e), where the blue areas stand for the stability domains in the (b, p_i) plane, and $b_{\rm cr}^{\rm low}$ and $b_{\rm cr}^{\rm upp}$ are lower and upper values of b for robust solitons. One finds that by increasing p_i, the scope of $[b_{\rm cr}^{\rm low}, b_{\rm cr}^{\rm upp}]$ progressively shrinks and merges at the $\mathcal{PT}$-symmetry-breaking point B ($p_i^{\rm cr} = 0.2$, $b_{\rm cr} = 1.39$) in Fig. 4(a). Beyond point B, this system cannot get stable vortex

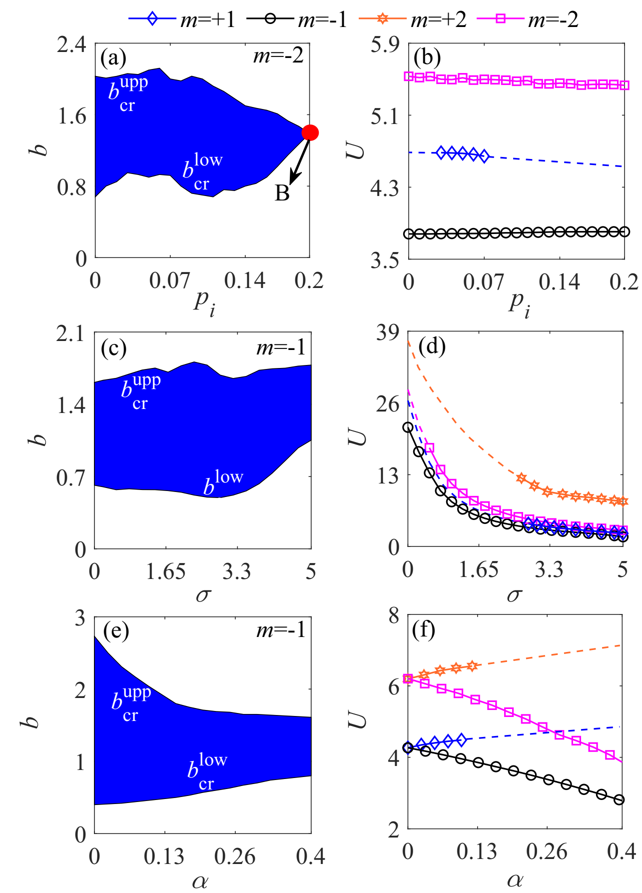

FIG. 4. Propagation constant b and power of six-core vortex LBs as functions of p_i (a), (b), nonlocal nonlinearity degree σ (c), (d), and rotation frequency α (e), (f). Point B in panel (a) stands for the critical point where b turns to complex. The solid and dashed lines represent the robust and unstable states. The fixed parameters are $p_r = 3$, $p_i = 0.1$, $\sigma = 2.5$, and $\alpha = 0.15$.

solitons (or pure real b) when $p_i > 0.2$. On the other hand, the scope $[b_{\rm cr}^{\rm low}, b_{\rm cr}^{\rm upp}]$ as a function of σ and α in Figs. 4(c) and 4(e) shows a milder tendency. The scope initially increases slightly and then decreases as the nonlocal coefficient σ increases. Furthermore, it decreases with the rotation frequency α.

The power of six-core vortex LBs can be determined by system parameters such as p_i, σ, and α, as shown in Figs. 4(b), 4(d), and 4(f), respectively. It is found that the power almost does not change with the increase of p_i. When p_i is beyond stability domains, the eigenvalues become complex and the vortex LBs with robust power cannot be obtained (depicted by the dashed lines or outside the axis scales). The power U decreases monotonically with the increase of σ [Fig. 4(d)], indicating that the power needed to maintain the robust vortex LBs in a Rydberg-dressed nonlinear atom system becomes smaller with the strengthening of the nonlocal degree [20,22].

In rotational atomic system, the U-α relation of vortex LBs has opposite rules with different signs of topological charges, i.e., ${\rm d}U/{\rm d}\alpha > 0$ with positive m ($m = +1$ and $+2$), and ${\rm d}U/{\rm d}\alpha < 0$ with negative m ($m = -1$ and -2) [Fig. 4(f)]. This phenomenon can be attributed to the nonequivalent distribution of gain/loss along the azimuthal direction [51]. On

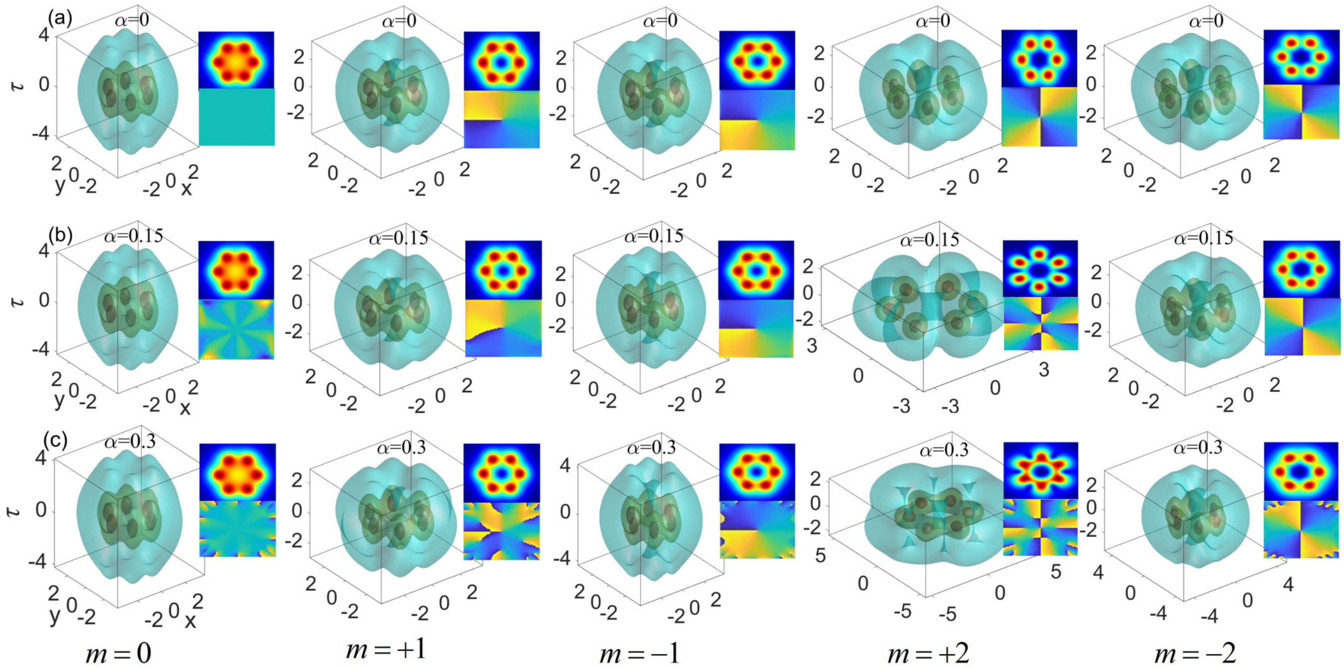

FIG. 5. Profiles of six-core vortex LBs in (x, y, τ) space with $\alpha = 0$, 0.15, and 0.3 and $m = 0$, ± 1, and ± 2. The moduli of three isosurface layers are 85%, 50%, and 5% of the maximum values $|\psi|_{\max}$, respectively. The insets are the corresponding projection and phase distributions in the (x, y) plane. The other parameters are $p_r = 3$, $p_i = 0.1$, and $\sigma = 2.5$.

the other hand, the rotation frequency is taken as $\alpha > 0$, a counterclockwise rotation according to Eq. (4). The Coriolis force of the pulse increases the power of vortex LBs [36,37,51,52]. As is well known, the phase of the vortex LBs has a counterclockwise rotation with $m > 0$ and a clockwise rotation with $m < 0$. The power of the solitons as well as the Coriolis force would be enhanced (reduced) when $m > 0$ ($m < 0$). The induction of α changes the stability of vortex solitons and enriches their modulation diversity as the states with the opposite charges degenerate by the introducing of rotation frequency, similar to the case of vortex solitons in twisted waveguide arrays without $\mathcal{PT}$ symmetry [37]. Thus, the optimal frequency for observing robust vortex solitons with various topological charges is $\alpha = 0.1$. Exceeding this value, the stability domains of the vortex solitons would be relatively small, especially for the topological charge $m = +2$.

The physics lies in the superposition of the orbital angular momentum of the vortices and the artificial angular momentum induced by the twisted waveguide arrays. In principle, vortex solitons with lower angular momentum are more stable than those with higher angular momentum. Thus, the rotational direction of waveguide arrays can weaken or strengthen the stability of vortex solitons with opposite charges.

Typical examples of six-core vortex LBs with different rotation frequencies and topological charges are shown in Fig. 5, where fundamental LBs are also presented for comparison. As α increases, the profiles do not show any significant differences and the phase structures exhibit a gradual distortion. According to the phase structures, vortex LBs are more unstable with positive topological charges or larger rotation frequencies. This phenomenon is more obvious when $m = +2$, as the profile expands dramatically with the increase of α due to the Coriolis force, agreeing well with the U-α relation in Fig. 4(f). For physical reasons, the Coriolis force and $\mathcal{PT}$ topological symmetry contribute to this distortion of profiles and phase structures.

B. Propagation and power current of six-core vortex LBs

To validate the predictions of the linear-stability analysis, we have performed extensive propagation simulations of six-core vortex LBs with different topological charges, by means of the split-step Fourier method with absorptive boundary conditions. The results are illustrated in Fig. 6. One finds that the robustness of the vortex structures varies depending on the sign of the topological charges. The profiles illustrate that vortices with positive charge ($m > 0$) are more prone to degenerate. This is evident since the core number gradually decreases from 6 to 3, ultimately resulting in the collapse of the vortex LBs, as illustrated in Figs. 6(a) and 6(b).

On the other hand, vortex LBs with $\alpha > 0$ and $m < 0$ maintain a dynamic equilibrium and propagate stably during propagation, as depicted in Figs. 6(c) and 6(d). As they propagate, the intensities of the cores display a periodic cycle with four steps: (i) equal distribution [Fig. 6(d1)], (ii) alternating distribution [Fig. 6(d2)], (iii) recovering to equal distribution [Fig. 6(d3)], and (iv) alternating distribution in the opposite sites [shown in Fig. 6(d4)]. This phenomenon is referred to a necklace breather (NB) whose cycle is $\Delta z = 180$. It is noteworthy that this NB effect occurs after a certain propagation distance, i.e., $z = 500$. Movies of six- and eight-core NBs can be found in the Supplemental Material [54] more directly.

The vortex LBs can be considered as a molecule of free-standing solitons rotating around the waveguide axis, which is similar to the gyrating solitons in a necklace of optical waveguides with $\mathcal{PT}$-symmetric fashion [62]. However, there are mainly three differences.

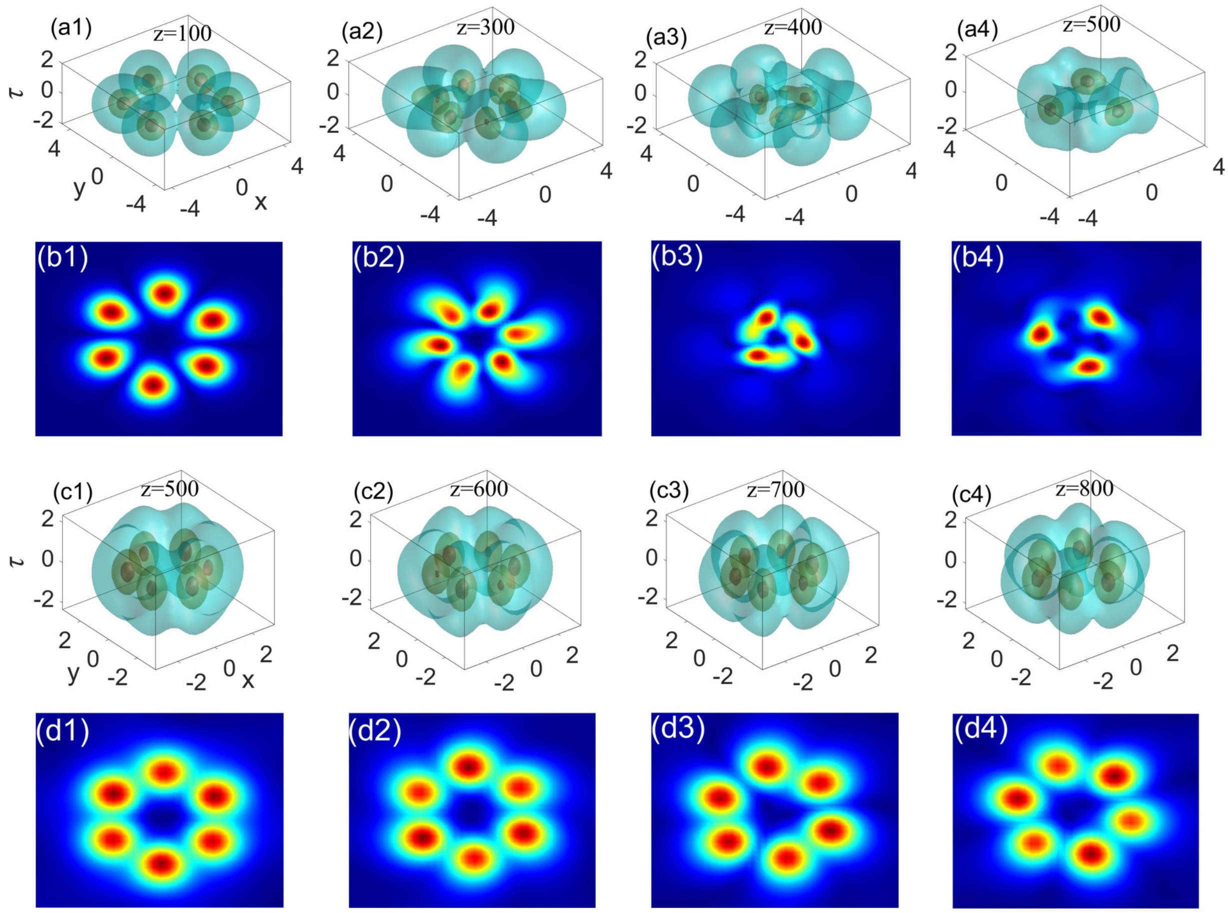

FIG. 6. Propagation of six-core vortex LBs along the propagation distance z with (a), (b) $m = +2$ and $z = 100$, 300, 400, and 500, and (c), (d) $m = -2$ and $z = 500$, 600, 700, and 800. The moduli of three isosurface layers are 85%, 50%, and 5% of the maximum values, respectively. The projections of moduli in the (x, y) plane are shown in the second and fourth rows. The other parameters are $p_r = 3$, $p_i = 0.1$, $\sigma = 2.5$, and $\alpha = 0.1$.

(i) The main equation (1) represents an uncoupled equation in which ψ can describe all the states in every waveguide, whereas in Ref. [62] each waveguide is associated with coupled wave functions $\psi_n (n = 1, \ldots, N)$.

(ii) The coordinates in our system rotate with frequency α, while solitons gyrate around the necklace by switching from one waveguide to the next in Ref. [62].

(iii) There exists a distinction between the gain and loss factors.

During the propagation of vortex LBs, energy is transferred from the core to the surrounding media, where it is stored. Subsequently, after traversing a certain distance, the stored energy is released back into the core. This recurring energy exchange is influenced by various factors, such as the rotation of coordinates and topological charges. The presence of an NB implies a power flow between the media and cores, which highlights its potential applications as light switch and storage.

To investigate the effect of power current on the stablility of vortex LBs in this 3D rotational system, we define the transverse power current as $\vec{S} = \frac{1}{2}(\psi \nabla \psi^* - \psi^* \nabla \psi)$. Here, $\psi = \varphi \exp(im\theta)$ is the solution of Eq. (5). The power current between neighboring cores is depicted in Fig. 7, using both nontwist ($\alpha = 0$) and twist system ($\alpha = 0.1$) configurations.

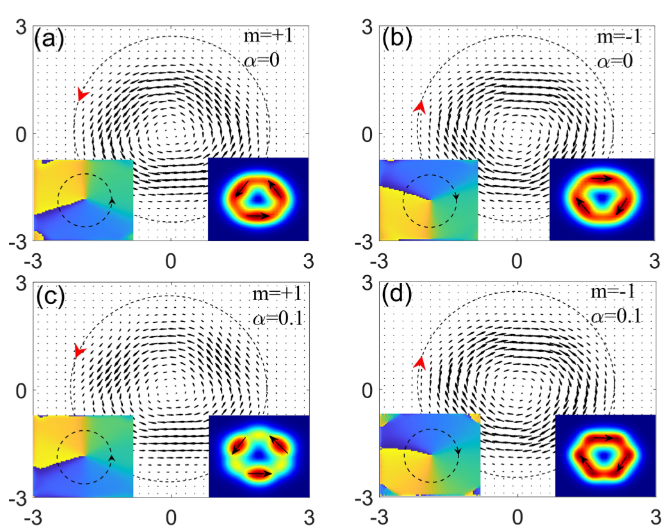

FIG. 7. Power current of six-core vortex LBs with $m = \pm 1$ and $\alpha = 0$ and 0.1. The red arrow represents the direction of the power current. The insets are the direction of phase structure and the modulus of power current $|S|$. The other parameters are $p_r = 3$, $p_i = 0.1$, and $\sigma = 2.5$.

The left and right parts of each panel illustrate the direction of the phase gradient (global current) and the power current from gain to loss in adjacent cores (local current). Notably, the global current is influenced by topological charges, while the local current indicates the direction of transfer from gain to loss between the nearest waveguide, as depicted in the imaginary part of potentials in Figs. 1(c) and 1(d).

Based on global and local currents, the power current $\vec{S}$ exhibits an anticlockwise (clockwise) rotation with $m = +1(-1)$, as illustrated by the red arrows in Fig. 7. The global and local currents flow in the same direction [Figs. 7(a) and 7(b)], which is different from the partially $\mathcal{PT}$-symmetric case [51]. We should note that the energy flux does not exhibit qualitative differences for varying p_i. The localization of the power current modulus is strengthened by the rotation of coordinates when $m > 0$ [Fig. 7(c)]. Furthermore, when considering the coordinate rotation, the modulus of the power current exhibits different distributions, depending on the sign of topological charges, see e.g., the right side of each panel in Figs. 7(c) and 7(d). This nonequivalence of two azimuthal directions arises in the rotational $\mathcal{PT}$-symmetric system and affects the generation, transformation, and stability of the vortex LBs.

IV. CONCLUSIONS

To summarize, we proposed a scheme for generating robust vortex LBs in a Rydberg atomic system under the modulation of twisted $\mathcal{PT}$-symmetric circular waveguide arrays. The proposed system employs a cold Rydberg-dressed four-level atomic configuration with an inverted-Y type structure. Robust vortex LBs can be observed with various topological charges. The vortex LBs with opposite charges exhibit different dynamics under the action of the Coriolis force. Particularly, the vortex LBs with negative topological charges exhibit broader stability domains compared to those with positive charges, due to the difference in azimuthal angle in the rotational configurations. Furthermore, the power decreases with the strengthening of nonlocal nonlinearities induced by the long-range Rydberg interactions. We found vortex solitons are robust even in the presence of gain and loss, i.e., $\mathcal{PT}$ symmetry. This finding was rarely reported in other PT-symmetric schemes. Our predictions may have applications in the light switch and storage devices.

Data will be made available upon reasonable request.

ACKNOWLEDGMENTS

This work is supported by the National Natural Science Foundation of China (Grant No. 62275075), the Science and Technology Research Program of Education Department of Hubei Province (Grant No. B2022188), the Natural Science Foundation of Hubei Province (Grant No. 2023AFC042), the Training Program of Innovation and Entrepreneurship for Undergraduates of Hubei Province (Grant No. S202210927003), and the Natural Science Basic Research Program in Shaanxi Province of China (Grant No. 2022JZ-02).

S.-L. Xu and J.-H. Li contributed equally to this work.

[1] Y. Silberberg, Collapse of optical pulses, Opt. Lett. **15**, 1282 (1990).

[2] L. Dong and Y. V. Kartashov, Rotating multidimensional quantum droplets, Phys. Rev. Lett. **126**, 244101 (2021).

[3] X. Jiang, Z. Fan, Z. Chen, W. Pang, Y. Li, and B. A. Malomed, Two-dimensional solitons in dipolar Bose-Einstein condensates with spin-orbit coupling, Phys. Rev. A **93**, 023633 (2016).

[4] H. Li, S.-L. Xu, M. R. Belić, and J.-X. Cheng, Three-dimensional solitons in Bose-Einstein condensates with spin-orbit coupling and Bessel optical lattices, Phys. Rev. A **98**, 033827 (2018).

[5] X. F. Zhang, L. Wen, L. X. Wang, G. P. Chen, R. B. Tan, and H. Saito, Spin-orbit-coupled Bose gases with nonlocal Rydberg interactions held under a toroidal trap, Phys. Rev. A **105**, 033306 (2022).

[6] D. Mihalache, D. Mazilu, F. Lederer, and Y. S. Kivshar, Collisions between discrete surface spatiotemporal solitons in nonlinear waveguide arrays, Phys. Rev. A **79**, 013811 (2009).

[7] B. A. Malomed, D. Mihalache, F. Wise, and L. Torner, Spatiotemporal optical solitons, J. Opt. B **7**, R53 (2005).

[8] Y. S. Kivshar and G. P. Agrawal, *Optical Solitons: From Fibers to Photonic Crystals* (Academic Press, San Diego, 2006).

[9] D. Mihalache, Multidimensional localized structures in optics and Bose-Einstein condensates: A selection of recent studies, Rom. J. Phys. **59**, 295 (2014).

[10] B. A. Malomed, Multidimensional solitons: Well-established results and novel findings, Eur. Phys. J. Spec. Top. **225**, 2507 (2016).

[11] L. Berge, Wave collapse in physics: Principles and applications to light and plasma waves, Phys. Rep. **303**, 259 (1998).

[12] Y. V. Kartashov, B. A. Malomed, and L. Torner, Solitons in nonlinear lattices, Rev. Mod. Phys. **83**, 247 (2011).

[13] L. Torner and Y. V. Kartashov, Light bullets in optical tandems, Opt. Lett. **34**, 1129 (2009).

[14] L. Song, Z. Yang, X. Li, and S. Zhang, Controllable Gaussian-shaped soliton clusters in strongly nonlocal media, Opt. Express **26**, 19182 (2018).

[15] A. S. Reyna, G. Boudebs, B. A. Malomed, and C. B. de Araújo, Robust self-trapping of vortex beams in a saturable optical medium, Phys. Rev. A **93**, 013840 (2016).

[16] I. B. Burgess, M. Peccianti, G. Assanto, and R. Morandotti, Accessible light bullets via synergetic nonlinearities, Phys. Rev. Lett. **102**, 203903 (2009).

[17] H. Sakaguchi and B. A. Malomed, Solitons in combined linear and nonlinear lattice potentials, Phys. Rev. A **81**, 013624 (2010).

[18] P. Grelu, J. M. Soto-Crespo, and N. Akhmediev, Light bullets and dynamic pattern formation in nonlinear dissipative systems, Opt. Express **13**, 9352 (2005).

[19] V. Skarka and N. B. Aleksic, Stability criterion for dissipative soliton solutions of the one-, two-, and three-dimensional complex cubic-quintic Ginzburg-Landau equations, Phys. Rev. Lett. **96**, 013903 (2006).

[20] B. B. Li, Y. Zhao, S. L. Xu *et al.*, Two-dimensional gap solitons in parity-time symmetry moiré optical lattices with Rydberg-Rydberg interaction, Chin. Phys. Lett. **40**, 044201 (2023).

[21] M. W. Chen, H. J. Hu, M. Zhu *et al.*, Weak-light solitons and their active control in Rydberg-dressed parity-time symmetry moiré optical lattices, Results Phys. **48**, 106392 (2023).
[22] Q. Y. Liao, H. J. Hu, M. W. Chen *et al.*, Two-dimensional spatial solitons in optical lattices with Rydberg-Rydberg interaction, Acta Phys. Sin. **72**, 104202 (2023).
[23] Y. Zhao, Y. B. Lei, Y. X. Xu, S. L. Xu, H. Triki, A. Biswas, and Q. Zhou, Vector spatiotemporal solitons and their memory features in cold Rydberg gases, Chin. Phys. Lett. **39**, 034202 (2022).
[24] Y. W. Guo, S. L. Xu, J. R. He, P. Deng, M. R. Belić, and Y. Zhao, Transient optical response of cold Rydberg atoms with electromagnetically induced transparency, Phys. Rev. A **101**, 023806 (2020).
[25] Z. Bai, W. Li, and G. Huang, Stable single light bullets and vortices and their active control in cold Rydberg gases, Optica **6**, 309 (2019).
[26] B. Liao, S. Li, C. Huang, Z. Luo, W. Pang, H. Tan, B. A. Malomed, and Y. Li, Anisotropic semivortices in dipolar spinor condensates controlled by Zeeman splitting, Phys. Rev. A **96**, 043613 (2017).
[27] A. B. Aceves, C. De Angelis, A. M. Rubenchik, and S. K. Turitsyn, Multidimensional solitons in fiber arrays, Opt. Lett. **19**, 329 (1994).
[28] A. B. Aceves, G. G. Luther, C. De Angelis, A. M. Rubenchik, and S. K. Turitsyn, Energy localization in nonlinear fiber arrays: Collapse-effect compressor, Phys. Rev. Lett. **75**, 73 (1995).
[29] D. Mihalache, D. Mazilu, F. Lederer, Y. V. Kartashov, L.-C. Crasovan, and L. Torner, Stable three-dimensional spatio-temporal solitons in a two-dimensional photonic lattice, Phys. Rev. E **70**, 055603(R) (2004).
[30] H. Leblond, B. A. Malomed, and D. Mihalache, Three-dimensional vortex solitons in quasi-two-dimensional lattices, Phys. Rev. E **76**, 026604 (2007).
[31] H. Leblond, B. A. Malomed, and D. Mihalache, Spatio-temporal vortex solitons in hexagonal arrays of waveguides, Phys. Rev. A **83**, 063825 (2011).
[32] D. Cheskis, S. Bar-Ad, R. Morandotti, J. S. Aitchison, H. S. Eisenberg, Y. Silberberg, and D. Ross, Strong spatiotemporal localization in a silica nonlinear waveguide array, Phys. Rev. Lett. **91**, 223901 (2003).
[33] S. Minardi, F. Eilenberger, Y. V. Kartashov, A. Szameit, U. Röpke, J. Kobelke, K. Schuster, H. Bartelt, S. Nolte, L. Torner, F. Lederer, A. Tünnermann, and T. Pertsch, Three-dimensional light bullets in arrays of waveguides, Phys. Rev. Lett. **105**, 263901 (2010).
[34] F. Eilenberger, K. Prater, S. Minardi, R. Geiss, U. Röpke, J. Kobelke, K. Schuster, H. Bartelt, S. Nolte, A. Tünnermann, and T. Pertsch, Observation of discrete, vortex light bullets, Phys. Rev. X **3**, 041031 (2013).
[35] W. J. Firth and D. V. Skryabin, Optical solitons carrying orbital angular momentum, Phys. Rev. Lett. **79**, 2450 (1997).
[36] C. Milián, Y. V. Kartashov, and L. Torner, Robust ultrashort light bullets in strongly twisted waveguide arrays, Phys. Rev. Lett. **123**, 133902 (2019).
[37] L. Dong, Y. V. Kartashov, L. Torner, and A. Ferrando, Vortex solitons in twisted circular waveguide arrays, Phys. Rev. Lett. **129**, 123903 (2022).
[38] C. M. Bender, Making sense of non-Hermitian Hamiltonians, Rep. Prog. Phys. **70**, 947 (2007).
[39] H. Hodaei, M.-A. Miri, M. Heinrich, D. N. Christodoulides, and M. Khajavikhan, Parity-time-symmetric microring lasers, Science **346**, 975 (2014).
[40] J. Yang, Partially PT-symmetric optical potentials with all-real spectra and soliton families in multidimensions, Opt. Lett. **39**, 1133 (2014).
[41] C. Hang, G. Huang, and V. V. Konotop, $\mathcal{PT}$ symmetry with a system of three-level atoms, Phys. Rev. Lett. **110**, 083604 (2013).
[42] Y. V. Kartashov, C. Hang, G. Huang, and L. Torner, Three-dimensional topological solitons in PT-symmetric optical lattices, Optica **3**, 1048 (2016).
[43] B. Peng, S. K. Ozdemir, F. Lei, F. Monifi, M. Gianfreda, G. L. Long, S. Fan, F. Nori, C. M. Bender, and L. Yang, Parity-time-symmetric whispering-gallery microcavities, Nat. Phys. **10**, 394 (2014).
[44] C. M. Bender and S. Boettcher, Real spectra in non-Hermitian Hamiltonians having $\mathcal{PT}$ symmetry, Phys. Rev. Lett. **80**, 5243 (1998).
[45] C. M. Bender, S. Boettcher, and P. N. Meisinger, PT-symmetric quantum mechanics, J. Math. Phys. **40**, 2201 (1999).
[46] H. Wang, S. Shi, X. Ren, X. Zhu, B. A. Malomed, D. Mihalache, and Y. He, Two-dimensional solitons in triangular photonic lattices with parity-time symmetry, Opt. Commun. **335**, 146 (2015).
[47] Z. Chen, J. Liu, S. Fu, Y. Li, and B. A. Malomed, Discrete solitons and vortices on two-dimensional lattices of PT-symmetric coupler, Opt. Express **22**, 29679 (2014).
[48] C. Hang, W. Li, and G. Huang, Nonlinear light diffraction by electromagnetically induced gratings with $\mathcal{PT}$ symmetry in a Rydberg atomic gas, Phys. Rev. A **100**, 043807 (2019).
[49] S.-L. Xu, N. Z. Petrovic, M. R. Belić, and Z. L. Hu, Light bullet supported by parity-time symmetric potential with power-law nonlinearity, Nonlinear Dyn. **84**, 1877 (2016).
[50] G. M. Li, A. Li, S. J. Su, Y. Zhao, G. P. Zhou, L. Xue, and S. L. Xu, Vector spatiotemporal solitons in cold atomic gases with linear and nonlinear PT symmetric potentials, Opt. Express **29**, 14016 (2021).
[51] Y. V. Kartashov, V. V. Konotop, and L. Torner, Topological states in partially-$\mathcal{PT}$-symmetric azimuthal potentials, Phys. Rev. Lett. **115**, 193902 (2015).
[52] L. Dong and C. Huang, Vortex solitons in fractional systems with partially parity-time-symmetric azimuthal potentials, Nonlinear Dyn. **98**, 1019 (2019).
[53] X. Zhang, F. Ye, Y. V. Kartashov, V. A. Vysloukh, and X. Chen, $\mathcal{PT}$-symmetry in nonlinear twisted multi-core fibers, Opt. Lett. **42**, 2972 (2017).
[54] See Supplemental Material at http://link.aps.org/supplemental/10.1103/PhysRevA.110.023508 for movies.
[55] N. V. Alexeeva, I. V. Barashenkov, A. A. Sukhorukov, and Y. S. Kivshar, Optical solitons in $\mathcal{PT}$-symmetric nonlinear couplers with gain and loss, Phys. Rev. A **85**, 063837 (2012).
[56] N. V. Alexeeva, I. V. Barashenkov, and Y. S. Kivshar, Solitons in $\mathcal{PT}$-symmetric ladders of optical waveguides, New J. Phys. **19**, 113032 (2017).

[57] I. V. Barashenkov, L. Baker, and N. V. Alexeeva, $\mathcal{PT}$-symmetry breaking in a necklace of coupled optical waveguides, Phys. Rev. A **87**, 033819 (2013).

[58] N. V. Alexeeva, I. V. Barashenkov, K. Rayanov, and S. Flach, Actively coupled optical waveguides, Phys. Rev. A **89**, 013848 (2014).

[59] J. Yang and T. I. Lakoba, Universally-convergent squared-operator iteration methods for solitary waves in general nonlinear wave equations, Stud. Appl. Math. **118**, 153 (2007).

[60] Y. V. Kartashov, A. Ferrando, A. A. Egorov, and L. Torner, Soliton topology versus discrete symmetry in optical lattices, Phys. Rev. Lett. **95**, 123902 (2005).

[61] L. Dong, D. Liu, Z. Du, K. Shi, and W. Qi, Bistable multipole quantum droplets in binary Bose-Einstein condensates, Phys. Rev. A **105**, 033321 (2022).

[62] I. V. Barashenkov and D. Feinstein, Gyrating solitons in a necklace of optical waveguides, Phys. Rev. A **103**, 023532 (2021).